



57Fe Mössbauer study of epitaxial TiN thin film grown on MgO(100) by magnetron sputtering

Qi, B.; Gunnlaugsson, H.P.; Mokhles Gerami, A.; Gislason, H.P.; Ólafsson, S.; Magnus, F.; Mølholt, Torben Esmann; Masenda, H.; Tarazaga Martín-Lueugo, A.; Bonanni, A.

Total number of authors:
18

Published in:
Applied Surface Science

Link to article, DOI:
[10.1016/j.apsusc.2018.09.107](https://doi.org/10.1016/j.apsusc.2018.09.107)

Publication date:
2019

Document Version
Peer reviewed version

[Link back to DTU Orbit](#)

Citation (APA):

Qi, B., Gunnlaugsson, H. P., Mokhles Gerami, A., Gislason, H. P., Ólafsson, S., Magnus, F., Mølholt, T. E., Masenda, H., Tarazaga Martín-Lueugo, A., Bonanni, A., Krastev, P. B., Masondo, V., Unzueta, I., Bharuth-Ram, K., Johnston, K., Naidoo, D., Schell, J., & Schaaf, P. (2019). 57Fe Mössbauer study of epitaxial TiN thin film grown on MgO(100) by magnetron sputtering. *Applied Surface Science*, 464, 682-691. <https://doi.org/10.1016/j.apsusc.2018.09.107>

General rights

Copyright and moral rights for the publications made accessible in the public portal are retained by the authors and/or other copyright owners and it is a condition of accessing publications that users recognise and abide by the legal requirements associated with these rights.

- Users may download and print one copy of any publication from the public portal for the purpose of private study or research.
- You may not further distribute the material or use it for any profit-making activity or commercial gain
- You may freely distribute the URL identifying the publication in the public portal

If you believe that this document breaches copyright please contact us providing details, and we will remove access to the work immediately and investigate your claim.

Accepted Manuscript

Full Length Article

^{57}Fe Mössbauer study of epitaxial TiN thin film grown on MgO(100) by magnetron sputtering

B. Qi, H.P. Gunnlaugsson, A. Mokhles Gerami, H.P. Gislason, S. Ólafsson, F. Magnus, T.E. Møhlholt, H. Masenda, A. Tarazaga Martín-Luego, A. Bonanni, P.B. Krastev, V. Masondo, I. Unzueta, K. Bharuth-Ram, K. Johnston, D. Naidoo, J. Schell, P. Schaaf, the ISOLDE collaboration

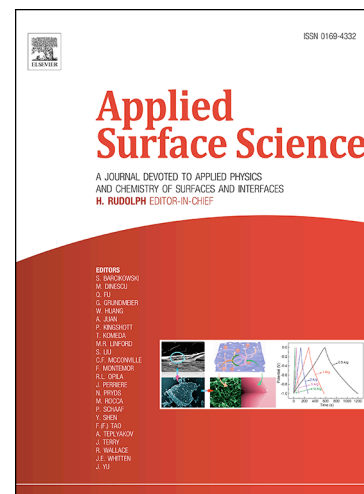
PII: S0169-4332(18)32523-6
DOI: <https://doi.org/10.1016/j.apsusc.2018.09.107>
Reference: APSUSC 40411

To appear in: *Applied Surface Science*

Received Date: 26 April 2018
Revised Date: 18 August 2018
Accepted Date: 12 September 2018

Please cite this article as: B. Qi, H.P. Gunnlaugsson, A. Mokhles Gerami, H.P. Gislason, S. Ólafsson, F. Magnus, T.E. Møhlholt, H. Masenda, A. Tarazaga Martín-Luego, A. Bonanni, P.B. Krastev, V. Masondo, I. Unzueta, K. Bharuth-Ram, K. Johnston, D. Naidoo, J. Schell, P. Schaaf, t. ISOLDE collaboration, ^{57}Fe Mössbauer study of epitaxial TiN thin film grown on MgO(100) by magnetron sputtering, *Applied Surface Science* (2018), doi: <https://doi.org/10.1016/j.apsusc.2018.09.107>

This is a PDF file of an unedited manuscript that has been accepted for publication. As a service to our customers we are providing this early version of the manuscript. The manuscript will undergo copyediting, typesetting, and review of the resulting proof before it is published in its final form. Please note that during the production process errors may be discovered which could affect the content, and all legal disclaimers that apply to the journal pertain.



^{57}Fe Mössbauer study of epitaxial TiN thin film grown on MgO(100) by magnetron sputtering

B. Qi¹, H. P. Gunnlaugsson¹, A. Mokhles Gerami², H. P. Gislason¹, S. Ólafsson¹, F. Magnus¹, T. E. Mølholt^{3,10}, H. Masenda⁴, A. Tarazaga Martín-Lueugo⁵, A. Bonanni⁵, P. B. Krastev⁶, V. Masondo^{7,12}, I. Unzueta⁸, K. Bharuth-Ram⁷, K. Johnston³, D. Naidoo⁴, J. Schell^{3,9}, P. Schaaf¹¹ and the ISOLDE collaboration³

1. Science Institute, University of Iceland, Dunhaga 3, IS-107 Reykjavík, Iceland
2. Department of Physics, K.N. Toosi University of Technology, PO Box 15875-4416, Tehran, Iran
3. PH Department, ISOLDE/CERN, 1211 Geneva 23, Switzerland
4. School of Physics, University of the Witwatersrand, Johannesburg, South Africa
5. Institut für Halbleiter-und-Festkörperphysik, Quantum Materials Group, Johannes Kepler University, Altenbergerstr. 69, Linz – Austria
6. Institute for Nuclear Research and Nuclear Energy, Bulgarian Academy of Sciences, 72, Tsarigradsko Chaussee Boulevard, Sofia, 1784, Bulgaria.
7. School of Physics, University of KwaZulu-Natal, Durban, South Africa
8. Dpto. Electricidad y Electronica, Universidad del Pais Vasco (UPV/EHU), CP. 644, 48080 Bilbao, Spain
9. Institute for Materials Science and Center for Nanointegration, Duisburg-Essen (CENIDE), University of Duisburg-Essen, D-45141 Essen, Germany
10. DTU Nutech, Risø Campus, Frederiksborgvej 399, Bygning 201, 4000 Roskilde, Denmark
11. Chair Materials for Electrical Engineering and Electronics, Institute of Materials Science and Engineering and Institute of Micro and Nanotechnologies MacroNano®, TU Ilmenau, Gustav-Kirchhoff-Straße 5, 98693 Ilmenau, Germany
12. Dep. of Chemistry and Dep. of Physics, Durban University of Technology, PO Box, 1334. Durban, 4000, South Africa

Abstract

The properties and performance of TiN thin films are closely related to the concentration and mobility of lattice defects in the thin film structures of TiN. This makes a local atomic scale study of TiN thin films an ever-growing demand. Emission ^{57}Fe Mössbauer spectroscopy (eMS) is a powerful tool in this regard, which we apply here to study an ultrathin TiN film epitaxially grown on MgO (100). With the help of theoretical calculations, our results show that most implanted Fe ions adopt a 2^+ valence state and locate at the Ti sublattice in the bulk-like single crystalline grains, with the rest Fe residing at the grain boundaries as interstitials. A small percentage of nitrogen point defects (vacancy V_{N} and interstitial N_{I}) are observed in the bulk-like crystalline grains. A temperature-dependent, interstitial N_{I} mediated site-exchange between N_{I} and V_{N} inside the crystal grain are deduced via a N_2 dimmer like diffusion of N_{I} through the crystal grains in the temperature range of 540 - 620 K. This is interesting in the perspective of exploring the catalytic property of TiN nanostructures. The titanium vacancy (V_{Ti}) is only detected at the grain boundaries. Annealing up to 813 K, both the V_{N} and N_{I} are annihilated in the crystalline grains and the V_{Ti} is fully recovered with healing of the grain boundaries. However, no evidence of ferromagnetism due to dilute implantation of $^{57}\text{Mn}/^{57}\text{Fe}$ and or structural defects in the film is obtained.

This suggests that the so far reported dilute magnetism and defect-induced ferromagnetism in TiN nanostructures requires a further systematic investigation.

Key words: TiN, Mössbauer spectroscopy, epitaxial thin film, defects

1. Introduction

As a prototype transition-metal nitride (TMN), TiN is an important material in hard coatings and modern microelectronics [1] [2]. It possesses excellent hardness, chemical stability, high melting temperature, appealing tuneable optical and electrical properties, such as the unique metallic behaviour in the visible and near-IR ranges [3] as well a disorder-induced metal-insulator transition properties [4]. TiN thin films have been widely used as wear- and corrosion-resistant coatings, diffusion barriers, gate electrodes in field-effect transistors (FET), as replacement of polycrystalline Si in large-scale integrated circuits, contact layers in solar cells, metal-insulator-superconductor (MIS) tunnel junctions [5] [6] [7] and low-loss plasmonic materials [8]. Furthermore, TiN is known to have a low electromagnetic loss at microwave frequencies and has found applications in low-loss superconducting qubits, microwave resonators for qubits and microwave kinetic inductance detectors [9] [10]. Recently, anomalous defect-induced magnetic and electromagnetic properties have been reported for both as-prepared and Fe-doped TiN nanocrystals [10] [11], although bulk TiN is non-magnetic. This renders TiN an appealing material for multi-functional ferromagnetic materials in spintronic applications.

TiN thin films can be synthesized by various deposition methods. Magnetron sputtering has proved to be a successful technique promoted to an industrial scale for many years [12], including the growth of advanced functional thin films used for solar cells in recent years [13] [14]. TiN stabilizes in the face centred cubic (FCC) structure. However, non-stoichiometry and possible structural defects commonly exist in TiN thin films grown by magnetron sputtering. The stoichiometry and microstructure defects in TiN have profound effects on the above-mentioned mechanical, electrical, optical, local magnetic and electromagnetic properties [15] [16] [17]. Especially with the ever-growing interest in the application of nanoscale materials in various quantum device architectures, atomic scale characterization of the material composition and microstructure defects is highly desirable in order to tune the material properties for the appropriate applications. Mössbauer spectroscopy is particularly useful in this regard, due to its sensitivity to the immediate atomic environment of the probe nucleus through electric interaction and magnetic hyperfine interaction (up to second next nearest neighbours) [18]. Using implantation of

radioactive parent isotopes (emission Mössbauer spectroscopy, eMS) in the sample of interest, one can study extremely dilute levels ($<10^{-3}$ at%) [19]. With eMS, the dilute Fe atoms in ZnO/AlN/GaN were confirmed in a paramagnetic state, ruling out the assumption of ordered magnetic origin of the dilute magnetic properties in ZnO/AlN/GaN [20] [21] [22].

Conventional ^{57}Fe Mössbauer spectroscopy was used to test the assumption about the occupation of excess nitrogen in the tetrahedral voids of TiN (B1) structures and annealing-assisted diffusion contribution to the intrinsic stress of the (Ti, Fe)N coating [23]. The spectroscopy was also carried out on Ti films and TiN coatings following a room temperature (RT) implantation of ^{57}Fe ions with an energy of 70 keV and a dose of 2×10^{16} Fe ions/cm² [24]. The implanted ^{57}Fe ions were found to individually occupy the local Ti sites forming α -Ti(Fe) and β -Ti(Fe) structures in the Ti foil. In the TiN coating, three components were identified: the first component ($\sim 33\%$) was due to the implanted ^{57}Fe ions replacing the N sites surrounded by Ti neighbors, forming structures like α -Ti(Fe) and β -Ti(Fe); the second, which was the main component, appeared as the Fe ions replacing the Ti atoms in the Fe₂N phase with Fe in regular lattice sites; the third component was in FeN phase, in which the Fe ions were located at highly perturbed sites at the grain boundaries. After annealing at 773 K in air, the Ti(Fe) phase transformed to the intermetallic Ti₂Fe compound. The Fe₂N phase was stable up to 873 K, whereas the FeN formed at the grain boundaries was converted to superparamagnetic α -Fe₂O₃, and gradually into magnetically ordered α -Fe₂O₃ due to oxidation. These early studies demonstrate that the ^{57}Fe Mössbauer spectroscopy is useful to follow compositional and structural changes of TiN coatings with doping, implantation and annealing of Fe ions. However, concerning the recent demand for atomic scale investigation of possible diluted or defect-induced magnetic properties of TiN nanostructures, a further ^{57}Fe Mössbauer spectroscopy study on up-to-date TiN structures with Fe doping at truly dilute level (a dose $< 2 \times 10^{16}$ Fe ions/cm²) is needed.

In this work, we employ ^{57}Fe eMS by implantation of short-lived radioactive $^{57}\text{Mn}^+$ ions in TiN at an extremely dilute level using the ISOLDE facility at CERN [25] [19]. This is especially powerful for atomic scale investigation of local structure defects and the possible diluted magnetic properties of TiN nanostructures. We chose an ultrathin (40 nm) epitaxial TiN film grown on a single crystalline MgO (100) substrate, which is an interesting gate stack system in future non-Si based metal-oxide-semiconductor devices. Furthermore, the epitaxial ultrathin TiN film, with well-defined grain boundaries and single crystalline grains/nanostructures, is ideal for studying annealing-induced structural changes and possible defect-related magnetic properties of the TiN at the atomic scale. The eMS results are then

compared with calculations using density functional theory (DFT) within the Wien2K package [26] for interpretation of spectral components.

2. Material and experimental method

The TiN thin film was grown on a single-crystalline MgO(100) at 400 °C by reactive magnetron sputtering with a Ti target (99.99%) in an argon (Ar, 99.999%) and nitrogen (N₂, 99.999%) gas mixture (20:1) at 0.4 Pa with an applied power of 100 W. The film shows epitaxial single crystalline cubic (fcc) TiN (100) structure as shown by the X-ray diffraction (XRD) in Fig.1 and with a low roughness at a thickness of 40 nm. The lattice parameter is around 4.248 Å, larger than that of a bulk TiN crystal (4.242 Å) due to compressive strain [27].

The ⁵⁷Fe eMS experiments were carried out at the ISOLDE facility at CERN. ⁵⁷Mn⁺ ($T_{1/2} = 90$ s) beams were produced by 1.4 GeV proton-induced fission in a heated UC₂ target followed by an element-selective laser ionization [28]. With acceleration to 50 keV and magnetic mass separation, a clean beam of ⁵⁷Mn⁺ with the intensity of a few times 10⁸ ⁵⁷Mn⁺/s was obtained. The ⁵⁷Mn⁺ ions were then implanted into the TiN (100) thin film on the MgO (100) substrate at an incident angle θ_1 of 30° relative to the sample surface normal.

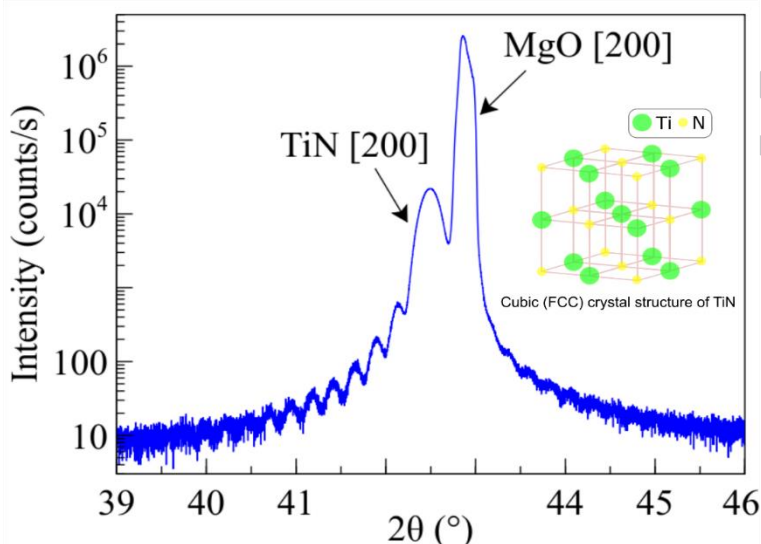


Fig.1: XRD (θ - 2θ) scans of the epitaxial TiN (100) thin film grown on MgO (100) substrate at 400 °C with DC magnetron sputtering. Inset: cubic (FCC) crystal structure of TiN.

⁵⁷Fe eMS spectra were recorded using a single line parallel plate avalanche detector (PPAD) equipped with an ⁵⁷Fe-enriched stainless steel electrode, mounted on a conventional drive system outside the implantation chamber at emission angle θ_E of 60° relative to the sample surface normal and 90° relative to the beam direction. The system was calibrated using implantations into α -Fe foils. The intrinsic line-shape of the detector is best described with a Voigt profile having Gaussian broadening of 0.1 mm/s and Lorentzian broadening of 0.34 mm/s. In the analysis, lines were analysed with additional Gaussian broadening. Isomer-shifts and velocities are given relative to the centrum of the spectrum of α -Fe at RT.

The total implanted local concentration of $^{57}\text{Mn}^+$ was estimated to be less than 10^{-4} at.% based on the maximum implanted fluence ($\sim 2 \times 10^{12} \text{ }^{57}\text{Mn}^+/\text{cm}^2$). The sample was heated with a halogen lamp from the backside. In some cases, after implanting ^{57}Mn at the specified temperatures, the sample was swiftly removed from the implantation chamber and quenched in liquid nitrogen at ~ 110 K, to study the possible implantation-induced disorder in the sample before being annealed.

3. Computational method

Kohn-Sham equations were solved to calculate the nuclear hyperfine parameters for a series of Fe sites in different local electron environments in the face-centred cubic (fcc) lattice structure of TiN with experimental lattice constant. The general potential linear augmented plane wave (FP-LAPW) method [29] which is based on the density functional theory (DFT) was used to solve the Kohn-Sham equations in Wien2k Code [26]. In the calculations, the generalized gradient approximation (GGA) in the form of Perdew Burke Ernzerhof (PBE) [30] was applied for the exchange-correlation potential. The electronic configurations of the elements in TiN are Ti: $[\text{Ar}]3d^24s^2$ and N: $[\text{He}]2s^22p^3$. The electronic configuration of Fe is $[\text{Ar}]3d^64s^2$. In order to create these electronic configurations, a separation energy -7 Ry was taken as the boundary between the core electron wave functions and those of the valence electrons. The radii of the muffin tin atomic spheres of Ti, N and Fe were taken to be 2.18, 1.77, and 2.22 a.u., respectively. The atomic radii were chosen such that the mutual overlaps between all kinds of combination of interstitial and atomic spheres are within the permissible limit of the atomic-sphere approximation. The maximum value of the angular momentum quantum number for the wave function expansion inside the Muffin-tin spheres were confined to $l_{\text{Max}}=10$. The cut-off parameter, $(R_{\text{MT}}K_{\text{Max}})$ was set to 7.0, where R_{MT} is the smallest of all atomic sphere in the unit cell and K_{max} is the magnitude of the largest K vector in the plane wave expansion, while the charge densities were expanded as Fourier series up to $G_{\text{max}}=12$ (Ryd) $^{1/2}$. A supercell size of $2 \times 2 \times 2$ and a mesh of $(7 \times 7 \times 7)$ k-points in the irreducible part of the first Brillouin zone were used in the calculation. The self-consistent calculations process was repeated until the total energy converged to 0.0001 electron charge. In this approach, the isomer shift δ was calculated from the relative contact density ρ between the absorber and source isomers as [31]:

$$\delta = \alpha(\rho_A - \rho_s)$$

(1)

where, ρ_A and ρ_s are the charge densities at the nuclei in the absorber (A) and sample (S) material, respectively, and the body-centred cubic (bcc) lattice structure of Fe was considered as sample (S). α is calibration constant, which was set to $\alpha = -0.29$ a.u.³·mm/s [32].

The quadrupole splitting ΔE_Q was obtained from the principal component V_{zz} of the electric field gradient. The electric field gradient tensor (EFG), expressed by its principal component V_{zz} and the asymmetry parameter η , gives the quadrupole splitting as:

$$\Delta E_Q = \frac{eQV_{zz}}{2} \sqrt{1 + \eta^2/3} \quad (2)$$

where e is the elementary charge and $Q = 0.16 \times 10^{-28}$ m² [33] is the nuclear quadrupole moment of the 14.4 keV Mössbauer state of ⁵⁷Fe.

4. Results and discussions

4.1. Experimental and computational results

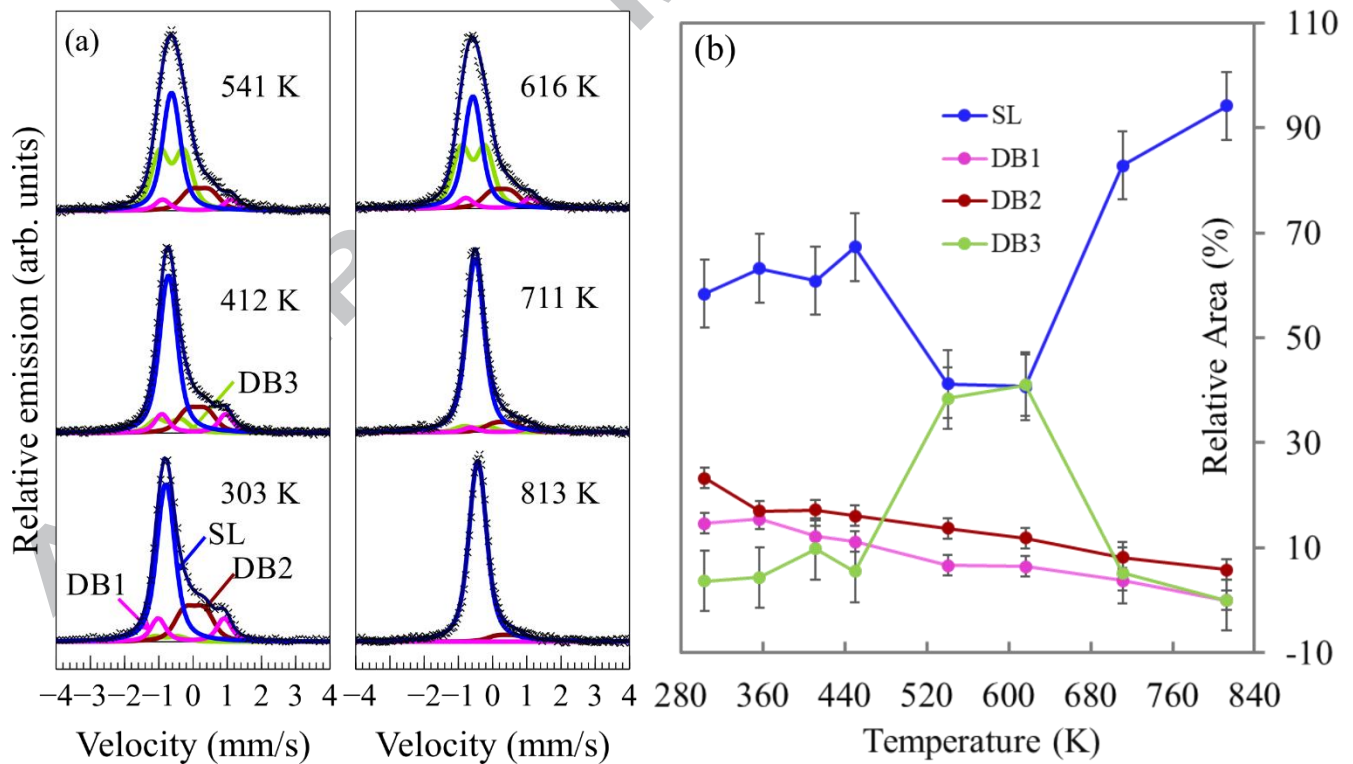


Fig.2: (a) ⁵⁷Fe eMS spectra of the TiN thin film after implantation of ⁵⁷Mn⁺ and (b) the corresponding area fractions of the components with the implantation temperature from 303 K to 813 K.

Fig.2(a) shows the selected ^{57}Fe eMS spectra obtained after implantation of ^{57}Mn into the TiN thin film in the temperature range of 303 - 813 K. The spectra were analysed using the program Vinda [34] with Voigt line shapes in accordance with the intrinsic line-shape of the detector.

The spectra are dominated by a single line (SL) with $\delta \sim 1$ mm/s, which is the main feature of the spectrum obtained at 813 K. By extrapolating the position of this line at 813 K to RT using the second order Doppler (SOD) shift, it coincides nicely with the dominating single line of the spectrum obtained at RT.

The spectrum broadening within velocity range of $v = \sim -1.0$ to -0.5 mm/s at temperature < 813 K points to the presence of one or more prominent spectral component(s) with $\delta \sim 0.5$ -1 mm/s. However, fitting with single lines would lead to unphysical isomer-shifts, so more likely, these features are due to quadrupole split components with the left-hand legs underneath the dominating SL. Therefore, in the final analysis, a minimum of two components (DB1 and DB2) was required to obtain a sufficient description of the experimental data.

In the spectra obtained at 541 K and 616 K, the single-line SL appears broader than at both the lower and higher temperatures. This could be due to temperature dependent broadening of the SL or due to the presence of an additional spectral component. Both hypothesis were tested and adding a new quadrupole split component (DB3) with δ similar to that of SL was clearly favoured in fitting.

The final analysis was then performed simultaneously with the above mentioned four components, where the resonance position of each line was set to follow the temperature dependent-SOD shift and the Gaussian broadening of each line was assumed to be temperature independent. The fitting parameters at RT (303 K) are listed in Table 1. The relative area fraction of the individual component as a function of temperature is plotted in Fig.2(b).

Table 1: Summary of hyperfine parameters from the data fitting of eMS spectra in Fig.2(a) and suggested site assignment of the components. δ_{RT} and $(\Delta E_{\text{Q}})_{\text{RT}}$ refer to the isomer shift and the quadrupole splitting at room temperature (RT), respectively, σ refers to the additional Gaussian broadening of the spectral lines after subtracting the experimental line width of the detector (0.1 mm/s).

Component	δ_{RT} (mm/s)	$(\Delta E_{\text{Q}})_{\text{RT}}$ (mm/s)	σ (mm/s)	Suggested site assignment
SL	0.79(1)	0	0.073(5)	Substitutional Fe^{2+} on Ti in defect-free TiN cubic
DB1	0.05(2)	1.93(3)	0.02(1)	Interstitial Fe
DB2	-0.04(1)	0.57(1)	0.11(1)	Interstitial Fe
DB3	0.79(4)	0.69(12)	0.07(2)	Substitutional Fe^{2+} on Ti in lattice-defect TiN cubic

As shown in Table 1, the additional Gaussian broadening of the lines (σ) are all very narrow, much lower than what is expected for amorphous environments ($\sigma \sim 0.3\text{-}0.4$ mm/s [35]). This suggests the good crystalline environments of the probe atoms.

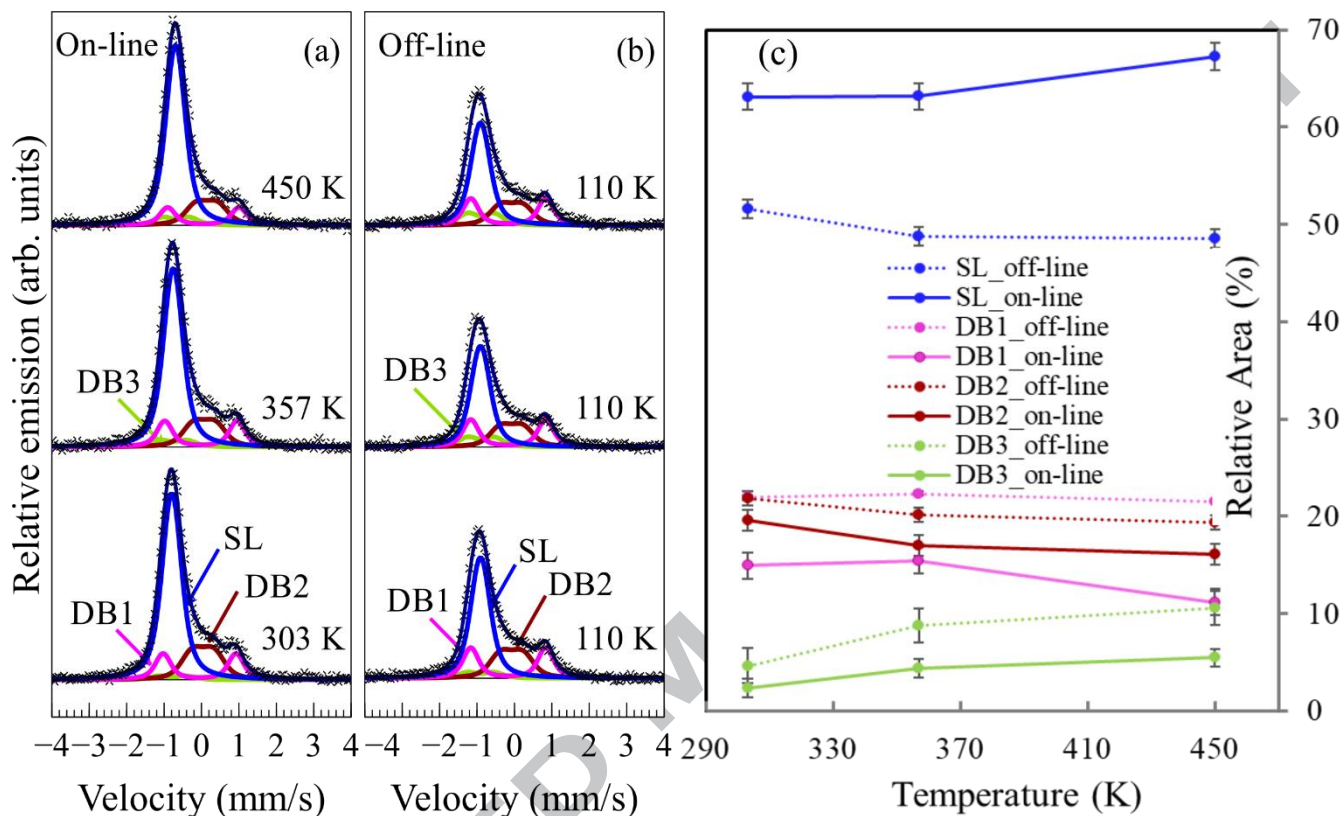


Fig 3: The ^{57}Fe eMS spectra measured (a) on-line during implantation and (b) off-line during quenching in the liquid nitrogen (110 K) after implantation of ^{57}Mn into the TiN thin film, and (c) the corresponding area fractions of the components at the indicate.

As shown in Fig.2(a) and Table 1, the dominant SL component with $\delta_{\text{RT}} \sim 0.8$ mm/s is characteristic of Fe^{2+} on a cubic site. The components DB1 and DB2 are characterized by the low δ_{RT} values (~ 0.0 mm/s) and significant $(\Delta E_{\text{Q}})_{\text{RT}}$ values (1.93 mm/s and 0.57 mm/s, respectively), which we tentatively assign to interstitial Fe (Fe_{I}) in highly-distorted lattice environment. They count for a minor part of the spectral area (less than 20%) at RT and decrease gradually with temperature. There is no evidence of an Fe^{3+} component, which would have shown a sextet type of spectrum due to slow paramagnetic relaxations. The doublet DB3 has similar δ_{RT} and σ values as the dominant SL, but with a larger $(\Delta E_{\text{Q}})_{\text{RT}}$ value of 0.69 mm/s. This suggests that the DB3 can also be considered as Fe^{2+} occupying a Ti sublattice site, but in a lattice defect environment. Furthermore, as shown in Fig.2(b), the changes in fractional areas of DB3 and SL with temperature follow an opposite trend. This indicates that there is a temperature-dependent dynamic site-exchange between SL and DB3. We will discuss this point in more detail in the next section.

Figs.3(a) and (b) show the ^{57}Fe eMS results obtained during on-line implantation at 303 K, 357 K and 450 K, and the spectra measured off-line upon rapid cooling in liquid nitrogen to ~ 110 K during the decay of ^{57}Mn after implantation at the temperatures specified above. The changes in the area fractions of the corresponding components are plotted with their error analyses in Fig.3(c). Except a notable reduction in the area fraction of the main component SL in the offline spectra due to the natural decay of the implanted ^{57}Mn isotope, there is no significant difference between the off-line and the on-line spectra. This confirms that the minor components are related to the intrinsic structural defects in the sample, indicating that the local lattice structure of TiN is preserved at the implantation temperature; the interstitials and vacancy defect sites have lower Debye temperatures than the dominant substitutional site.

The hyperfine parameters for different configurations of Fe on substitutional and interstitial sites in TiN were simulated, the results are summarized in Table 1s in Supplementary Material. As shown in Table 1s, although some of the calculated substitutional configurations can explain the SL and DB3 components, they cannot explain the components with isomer shift ~ 0.0 mm/s (DB1 and DB2). Because of the recoil imparted on the daughter ^{57}Fe atom in the β^- decay of ^{57}Mn or implantation directly on interstitial sites, looking for interstitial defects seems plausible. Therefore, the configurations with Fe atom as interstitials located at the centre of the cubic TiN lattice with and without V_{Ti} or V_{N} are also calculated and included in Table 1s. Comparison of the computational results and the eMS measurement results are shown in Table 2.

Table 2: Comparison between theoretical and experimental measured hyperfine parameters for substitutional (Fe_s) and interstitial (Fe_I) configurations (X denotes-not detected).

#	Calculated			Measured		
	δ (mm/s)	ΔE_Q (mm/s)	State	δ (mm/s)	ΔE_Q (mm/s)	Component
1	0.84	0	Fe_s	0.79(0)	0(0)	SL
2	0.76	0.16	$\text{Fe}_s\text{-}V_{\text{N}}$ ($d = 2.15 \text{ \AA}$)	x	x	x
3	0.69	0.06	$\text{Fe}_s\text{-}V_{\text{N}}$ ($d = 3.67 \text{ \AA}$)	x	x	x
4	0.65	0.03	$\text{Fe}_s\text{-}V_{\text{Ti}}$	x	x	x
5	0.74	0.17	$\text{Fe}_s\text{-}V_{\text{Ti}}\text{-}V_{\text{N}}$	x	x	x
6	0.53	0.26	$\text{Fe}_s\text{-}2V_{\text{N}}$ (90°)	x	x	x
7	0.82	0.69	$\text{Fe}_s\text{-}2V_{\text{N}}$ (180°)	0.79(4)	0.69(12)	DB3
8	0.71	0.25	$\text{Fe}_s\text{-}V_{\text{N}}\text{-}N_{\text{I-cubic center}}$	x	x	x
9	0.79	0.03	$\text{Fe}_s\text{-}N_{\text{I-cubic center}}$	x	x	x

10	-0.01	0.03	Fe _I -cubic center	x	x	x
11	-0.06	1.34	Fe_I-cubic center -V_N	-0.04(1)	0.57(1)	DB2
12	0.01	1.10	Fe_I-cubic center -V_{Ti}	0.05(2)	1.93(3)	DB1

Table 2 shows that the Fe_s-defect-free cubic configuration (#1 in Table 2), which has $\delta = 0.84$ mm/s and $\Delta E_Q = 0$ mm/s, agrees well with the experimental values of the singlet line component SL, which has $\delta = 0.80$ mm/s and $\Delta E_Q = 0.0$ mm/s, respectively. The configuration Fe_s with two nitrogen vacancies at the angles of 180° (Fe_s-2V_N (180°), #7 in Table 2), which has calculated values of $\delta = 0.82$ mm/s and $\Delta E_Q = 0.69$ mm/s, is very close to the DB3 component which has been measured with $\delta = 0.79$ mm/s and $\Delta E_Q = 0.69$ mm/s, respectively.

4.2. Discussion

The single line (SL) fits reasonably well with the calculated results for Fe_s (#1 in Table 2). However, the calculated values for some of the vacancy type defects (#2-5 & #8-9 in Table 2) indicate that such defects might also contribute to the SL and could explain the slight broadening of the line. Only the Fe_s-2V_N (180°) (#7 in Table 2) gives rise to significant quadrupole splitting to explain the large ΔE_Q value of DB3 component.

The only defects found with isomer-shifts ~ 0 mm/s, are interstitial type of defects. Isolated interstitial atoms (#10 in Table 2) would give rise to a line without quadrupole splitting. Although such component could be buried within the DB2 component, in most cases, some sort of interstitial-vacancy defect complex is needed in order to account for the noticeable ΔE_Q values of DB1 and DB2. Furthermore, the calculated $\Delta E_Q = 1.10$ mm/s and 1.34 mm/s are not consistent with the measured $\Delta E_Q = 1.93$ mm/s and 0.57 mm/s values of component DB1 and DB2. To solve this

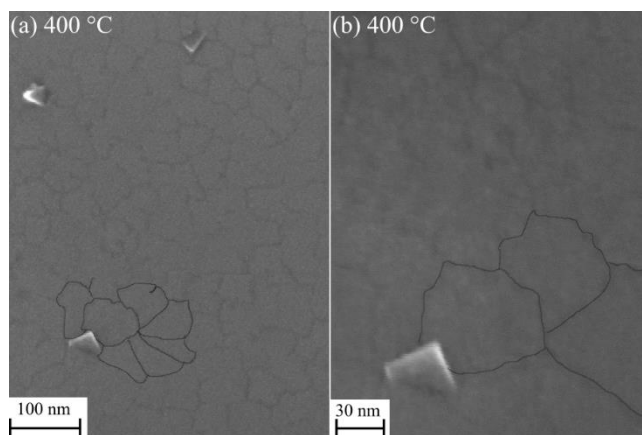


Fig.4: SEM images of TiN films. The scale bars are 100 nm and 30 nm, respectively. The dark-line contours are added as a guide to the eye to highlight grain boundaries. The triangle-shaped bright objects are (111)-faceted grains.

discrepancy, the particulate sceneries considered in the theoretical calculations and the sample conditions needed to be revisited.

Considering the thin film growth conditions, grain boundaries are commonly observed in thin films grown by magnetron sputtering on heterogeneous substrates [36]. Although our TiN thin film was

epitaxially grown on MgO (100), the growth did not follow an ideal layer-by-layer mode. With an established epitaxial relationship with MgO (100) substrate starting from growth temperature at 200 °C, the film grown at 400 °C is the result of purely geometrical development from growth at 200 °C, where the film is dominated with small flat rounded [200]-oriented grains about 14.8 nm wide and some (111)-faceted pyramidal grains scattered on the surface nm [27]. This means that on average there is a grain boundary in every 14.8 nm distance along the surface, which counts the grain density around 7% per nm. With growth temperature increasing to 400 °C, the faceted pyramidal grains rapidly give way to the dominant fast growth of large flat rounded grains, which reach a width of approximately 57.3 nm. Thus, on average, there is a grain boundary every 57.3 nm along the surface, i.e. with a grain boundary density of around 2% per nm. The grain boundaries are frequently seen on the TiN thin film as highlighted by the dark-lines added around the grains in the SEM images in Fig.4.

Based on the results in Table 2 and the TiN thin film growth conditions, we discuss the results in more details in the following subsections.

4.2.1. Site assignments for components SL and DB3

As illustrated in Fig.5(a), the implanted Fe atom occupies a Ti lattice site in a regular octahedral unit cell surrounded by six nearest N neighbour atoms (1, 2, 3, 4, 5 and 6). This gives a homogenous electron density distribution around the Fe atom and corresponds to the SL component measured by eMS, confidently assigned to the substitutional Fe_s on Ti sublattice site in defect-free cubic lattice environment. In Fig.5(b), the implanted Fe atom takes the Ti lattice site which is bonded only to four co-planar N atoms, with two vacant N sites (3' and 4'), perpendicularly aligned out-of-plane. This breaks the octahedral space-symmetry of the electron density distribution around the Fe atom, thus creating an appreciable ΔE_Q , in line with the hyperfine parameters of the component DB3, which counts for ~4% of the total spectral intensity at RT as shown in Fig.2(b).

However, as shown in Fig.2(b), it is surprising to observe that the area fraction/intensity of DB3 first increases from ~4% at 440 K to ~40% at 620 K, then reduces to 0% above 813 K. Corresponding changes in the area fraction/intensity of the SL component are also observed, but in the opposite direction. This points towards a temperature-dependent dynamic site-exchange between the occupied and the vacant N lattice sites in the TiN cubic structure. This can be explained in two possible ways, i.e. 1) the lattice N atoms become mobile and diffuses from occupied lattice site towards the vacant site, or 2) the implanted $^{57}\text{Mn}/^{57}\text{Fe}$ probe atoms have a higher tendency to be trapped into the lattice defect area with

V_N upon the lattice cascade damage, within the 90 s lifetime of ^{57}Mn atoms in the temperature range of 540-620 K. With temperature increasing further to 710 K and above 813 K, due to the high mobility of nitrogen interstitials, which finally fill up the nitrogen vacancies, thus resulting in the increasing of SL at the reduction of DB3. We try to discuss these two possibilities in more details as the following.

Based on the theoretical simulation results from the literature [37] [38] [39] and our sample growth conditions [27], we know that:

N atom diffuses significantly faster than the metal (Ti) atom and is thus expected to move by the vacancy (V_N , octahedral sites) diffusion mechanism in rock-salt cubic structure of TiN [40]. This means that the diffusivity of the N lattice atom is linked to the diffusion of V_N . V_N and N_I are regarded as the primary point defects in TiN. First-principles calculations [37] [38] found that diffusion of V_N and N_I are activated at different temperatures in a range of several hundreds of degrees, and are related to the interactions and migration of N point defects. The migration activation energy of V_N is as high as 3.8 eV. The large barrier indicates that V_N diffusion is activated only at very high temperatures. This practically means that the V_N is stationary in the experimental temperature range in our case.

In contrast to V_N vacancies, N_I tends to form N_I pair complexes in several stable configurations. N_I migration is relatively facile, tend to form low energy split-configurations with stretched N-N bonds with a substantial binding energy of 0.55 eV aligning along [111] and $[10\bar{1}]$ crystal directions, the latter is the minimum energy migration path. The calculated diffusion barriers (E_d) for isolated N_I and N_I pairs along $[10\bar{1}]$ directions are 1.3 eV and 2.0 eV, respectively. (These are very reasonable numbers for interstitial defects). This relatively low E_d value indicates that N_I diffusion can be activated at much lower temperatures than V_N [37], which may explain that the proportional changes of the SL and DB3 components can happen in the medium temperature range in our experiment.

Further study on diffusion of N vacancy and N self-interstitial point defects in TiN using *ab initio* and classical molecular dynamics (AIMD and CMD) simulations [39] confirmed that the most stable self-interstitial N_I position in TiN is a split-bond configuration formed with nitrogen lattice atoms. This can be treated as a N_2 dimer centered at an anion lattice site (N_I-N_{exc} , where N_{exc} refers to the lattice N atom pairing with N_I) with a N-N distance of 1.1 Å, which is about one third of the equilibrium N-N lattice distance (~ 3 Å) in TiN. After several random rotations around the N_I-N_{exc} center of mass, which is in the proximity of the original N lattice site, the N_I-N_{exc} bond breaks and one of the two N atoms permanently migrates to a neighboring anion site by passing through metastable eightfold-coordinated

tetrahedral positions, thus forming a N_I-V_N pair (Frenkel pair). This process yields temperature dependent N_I diffusion coefficients $D_I(T)$ with an exponential pre-factor $A^I = 7.28 (\times 1.8^{\pm 1}) \times 10^{-4} \text{ cm}^2 \text{ s}^{-1}$ and activation energy $E_a^I = (1.17 \pm 0.13) \text{ eV}$. As for V_N , it moves along [110] directions between neighboring N sites with much less mobility, yielding diffusion coefficients $D_V(T)$ with an exponential pre-factor $A^V = 3.89 (\times 2.5^{\pm 1}) \times 10^{-1} \text{ cm}^2 \text{ s}^{-1}$ and activation energy $E_a^V = (3.65 \pm 0.23) \text{ eV}$. Based on equation (4) in Ref. [39], a general expression for the temperature dependent diffusion coefficients of N_I and V_N as follows:

$$D_I(T) = 7.28(\times 1.8^{\pm 1}) \times 10^{-4} \times \exp^{[-1.17 \pm 0.13] \times 11604/T}$$

$$D_V(T) = 3.89(\times 2.5^{\pm 1}) \times 10^{-1} \times \exp^{[-3.65 \pm 0.23] \times 11604/T}$$

Based on the above equations, the diffusion coefficient and diffusion length within the lifetime of the Mn atom (90 s) of N_I and V_N at various annealing temperatures of the TiN thin film during eMS measurement can be calculated and listed in Table 3.

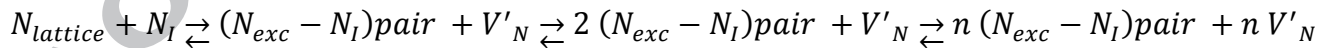
Table 3: Nitrogen self-interstitial (N_I) and nitrogen vacancy (V_N) diffusion coefficient and diffusion length at various annealing temperatures of TiN thin film during eMS measurement.

T (K)	Diffusion coefficient ($\text{cm}^2 \text{ s}^{-1}$)		Diffusion length (\AA) within the 90 s lifetime of the ^{57}Mn atom	
	N_I	V_N	N_I	V_N
540	$(0.3-79) \times 10^{-15}$	$(0.01-118) \times 10^{-35}$	1.6-27	$(0.03\sim 10) \times 10^{-9}$
620	$(0.1-46) \times 10^{-13}$	$(0.01-155) \times 10^{-30}$	9.9-204	$(0.06\sim 120) \times 10^{-7}$
710	$(0.2-17) \times 10^{-12}$	$(0.05-516) \times 10^{-27}$	46-389	$(0.06\sim 6.8) \times 10^{-5}$

Table 3 shows that at all temperatures, N_I diffusion coefficients are much larger than V_N by many orders of magnitude. This confirms that at the given annealing temperatures, V_N can be treated as stationary, whereas N_I is highly mobile.

Spontaneous formation and dissociation of N_I-V_N Frenkel pairs in a defect-free TiN is thermodynamically possible [39] and can be a perfect explanation on the conversion of SL to DB3 in our case. However, dynamically speaking, the probability of such event seems very rare with consideration that the annealing temperatures we used are far below the melting temperature of TiN. Therefore, some other factor is needed to support that the probability of spontaneous formation and annihilation of V_N under our experimental conditions during the 90 s lifetime of Mn atom is high enough to explain our data

concerning the conversion of SL to DB3 in the temperature range of 540-620 K. Here we propose that the extra factor is the pre-presence of isolated N_I in the lattice vacancy-free TiN. Indeed, as shown in Table 2, the hyperfine parameters for component #1 (SL, Fe_s) and component #9 (Fe_s-N_I) are very similar. This means that there is a portion of (Fe_s-N_I) component hidden in the SL (Fe_s) component, which is not distinguishable by eMS. The as-deposited TiN film in our case has lattice parameters around 4.248 Å, ~0.5–0.7% larger than the lattice constant of stoichiometric cubic structured TiN ($a = 4.242$ Å). This indicates that the concentration of N_I in the thin film is apparently higher than the one used for the CMD and AIMD simulations (which assume $a = 4.242$ and $N_I \sim 1\%$ of the total number of N atoms) [39]. There was also experimental evidence that the low-energy ion deposition like DC-magnetron sputtering can create N_I [41]. As shown in Table 3, owing to its low diffusion barrier and high diffusion coefficient, this portion of N_I can be thermally mobilized as the temperature increases from 540 K to 620 K and may create new defect structures in TiN. As it has been discussed above, the N_I tends to form a strong N-N bonds with the nitrogen lattice atoms in low energy split-configurations and diffuses through the energy minimum migration path along the $[10\bar{1}]$ direction. It is plausible that during migration, before each jump, the isolated N_I temporarily bonds with the nearest lattice N atom (N_{exc}) as a metastable $N_{exc}-N_I$ complex aligning along the $[10\bar{1}]$ direction. The $N_{exc}-N_I$ complex has binding energy of 0.55 eV and bond length of 1.1 Å, about one third of the equilibrium N-N lattice distance (~ 3 Å) in TiN [39]. This is quite a strong/tight bond comparing with the N-Ti bond in TiN. This means that the lattice N in the $N_{exc}-N_I$ pair would be temporarily carried away from its equilibrium lattice site in TiN cubic lattice as migration of N_I . Each formation of a $N_{exc}-N_I$ bond would create a metastable V'_N at the original N lattice site. In most cases, the N_{exc} and V'_N recombines within a fraction of ns; ~half of these processes result in the exchange of two nitrogen lattice atoms and creation of extra V_N . This is similar to a chain reaction of spontaneously formation/dissociation of ($N_{exc}-N_I$) pair accompanied by V_N creation/refilling, catalysed by the pre-presence of N_I species as the follow:



This equals a conversion of SL to DB3 with probability of $\sim 50\%$ [39] as N_I migrates along $[10\bar{1}]$ direction from one TiN cubic unit cell to the next unit cell in the temperature range of 540 K to 620 K. The probability increases exponentially with temperature. Above 700 K, the migration length of N_I within the lifetime of the ^{57}Mn atom (90 s) reaches 46 Å-400 Å distance, which is comparable to the typical grain size of the TiN thin film. With this diffusion length, the excess N_I inside the crystal grain could migrate all the way to the V_N sites or to the surface of the grain boundaries to be annihilated as N_2 .

The second possibility is that the implanted $^{57}\text{Mn}/^{57}\text{Fe}$ atoms preferably stop more in the V_N area than the defect-free area, upon the implantation-induced structural cascade damage in the temperature range of 540 - 620 K, thus leading to a higher portion of DB3 to be probed by eMS during the 90 s lifetime of ^{57}Mn atoms. With temperature increasing, the damage sites are annealed, and N_I diffuses to fill the V_N sites, which leads to a recovery of the SL component and a final disappearance of the DB3 component. However, as confirmed by the quenching results in Fig.3, there is no significant lattice damage to be found in eMS as a result of ^{57}Mn implanting from RT to 450 K. It is unlikely that more cascade damage would occur at 540 - 620 K. The minor components shown in the eMs were related to the intrinsic structural defects in the sample. Therefore, attributing the increase of DB3 to the preferable location of $^{57}\text{Mn}/^{57}\text{Fe}$ atoms in the cascade damage area is less supportable by the present data.

In summary, from both the experimental and the theoretical points of view, there exist mobile N_I atoms in the defect-free bulk-like phase of TiN thin films. The conversion of the SL component to the DB3 component can be the result of a diffusion of N_I coupled with the temporary creation of metastable V_N . With temperature increasing to 700 K and above 810 K, N_I diffuses to fill the intrinsic V_N sites in the bulk, or all the way to the grain boundary and surface of the thin film to be released as N_2 . This leads to a recovery of SL component and the final disappearance of the DB3 component. The overall process concerning the conversion of SL and DB3 based on the diffusion of N_I and refilling of V_N is schematically illustrated in Fig.5.

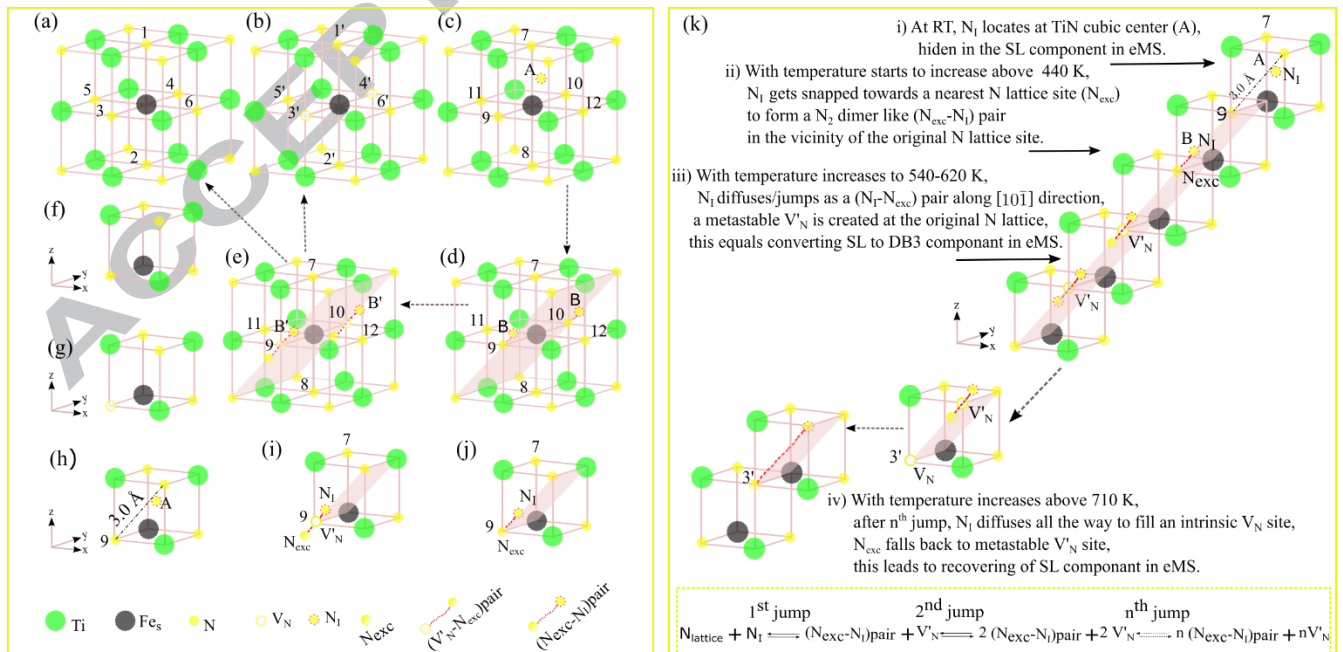


Fig.5: Schematic illustration of the local lattice configurations of substitutional Fe_s and the conversion of SL and DB3 in the experimental temperature range (303-810 K). In (a), the ⁵⁷Fe atom occupying a Ti lattice site bonded by six fully occupied nearest N atoms (1, 2, 3, 4, 5 and 6) represent component SL. Whereas in (b), among the six nearest N sites, the two N sites (3' and 4') which are arranged at 180° relative to each other, are vacant and represent component DB3. In (c), additional N_I, located at the cubic unit cell center A of TiN, is shown with the possibility to form a stretched (N_{exc}-N_I) pair like a N₂ dimer with the lattice N atom at site 9 or 10 and diffuses further away along the [10 $\bar{1}$] direction (shaded in color) as shown in (d and e), which is the most stable configuration and lowest energy migrating path of N_I [37]. At medium temperatures 540 K - 620 K, transition among configurations from (c) to (d), (e) and (b) by the formation of (N_{exc}-N_I) pairs and creation of metastable nitrogen vacancy (V'_N) is more likely. With temperature increasing from 710 K to above 810 K, with further diffusion of (N_{exc}-N_I) pairs, direct transition from (e) to (a) by healing metastable nitrogen vacancy (V'_N) with N_{exc} and filling of intrinsic V_N with N_I, is feasible. The related half unit cell structures of TiN cubic are shown in (f)-(j), respectively. The step-wise transition from (c) to (d) and back to (b) and (a) is detailed in (k). Solid green, yellow and black circles represent Ti, N lattice atoms and substitutional ⁵⁷Fe atoms on Ti lattice sites, respectively. Filled dotted and void solid yellow circles represent N_I and V_N, respectively. Note: the ⁵⁷Fe should be treated as ⁵⁷Mn in the context of immediate interaction of implanted atoms with the local crystal structures upon implantation. The bottom block shows the process by which V'_N was temporarily created as a result of N_I diffusing through the lattice defect-free area in a form of (N_{exc}-N_I) pair. This explains the area conversion between components SL and DB3 in eMS in the temperature range of 540 - 620 K.

4.2.2. Site assignments for components DB1 and DB2

Fig.6 illustrates the two configurations of Fe_I at the centre of a TiN cubic structure with V_{Ti} and V_N, respectively, in the grain boundary region. On account of the cubic structure, growth of TiN is generally controlled by the competition between the temperature-dependent fast lateral growth rate of the (200) oriented grains and the large geometric growth rate of the (111) oriented grains. In our case, the growth in (200) orientation is found favourable at 400 °C because of the epitaxial relationship with the substrate crystal structure [27]. Therefore, as shown in Fig.6(a), the (110) plane, which is a common side for both the (200) and (111) orientations, is chosen to represent the grain boundary. Based on the experimental evidence, oxygen can be introduced from remaining O₂ in the vacuum chamber (1.3×10^{-4} Pa) during deposition or exposure of the sample to air, and then reacts with Ti in TiN at the grain boundary and the surface to form oxides [17], [27], [42]. An ultrathin oxide passivation layer can be formed at an intermediate temperature and low partial oxygen pressure, where the temperature is high enough for the V_{Ti}, created upon initial oxidation, to diffuse away from the TiN/oxide interface, but too low to allow any substantial relaxation of the initially formed oxide islands into pseudo-amorphous and more reactive structures. The oxygen pressure is low enough to allow the oxidation to reach equilibrium. Under these conditions, the oxide layer formed is structurally ordered. It consists of -O-Ti- rows and represents a (1×1) surface unit cell, where vacancy segregation from bulk to the TiN/oxide interface is strongly

inhibited, and for the same reason, further oxide growth into the bulk is inhibited since it would require overcoming a high-energy barrier [43].

Under the conditions in which the TiN film of this study was grown, stored and post-annealed at temperature ranging from RT to 813 K, the formation of an ultrathin oxide passivation layer at the grain boundary and the surface is unavoidable. Theoretical modelling of surface oxidation of TiN [43] demonstrated that in the case of TiN (100), Ti vacancies form spontaneously during the initial oxidation reactions and remain underneath the resulting reconstructed oxides which form structurally stable -O-Ti-bridging rows, and has been observed experimentally [44] [45].

Based on the theoretical study and experimental results in Table 2, considering the magnetron sputtering thin film growth conditions, which tend to produce a TiN thin film with appreciable amount of grain boundaries (2%-7%) and ultrathin-surface-oxidation as mentioned above, we assign DB1 to the Fe_I located at the center of a cubic unit cell of TiN with V_{Ti} (#12 in Table 2) at the grain boundaries owing to oxidation of Ti atoms upon adsorption of O atoms. The process is schematically illustrated in Figs.6(b) and (d). Fig.6(b) illustrates the Fe_I in the center of the TiN cubic unit cell with a V_{Ti} (position 4) at the grain boundary, where the nearest-surface Ti atoms in TiN cubic structure close to the grain boundary have moved from the original positions (1, 2 and 3) outward to the boundary surface positions (1', 2' and 3') in TiO_4 tetrahedral structure underneath the -O-Ti- bridging rows as a result of oxidation of surface Ti atoms of TiN [43]. This enhances the distortion of the cubic symmetrical surrounding of the V_{Ti} . The Fe_I , which is either due to the implantation or the recoil-induced relocation of Fe ($\langle E_R \rangle = 40$ eV, $E_{R,Max} = 93$ eV), most likely stops at the grain boundaries. Comparing to the bulk phase, the Fe_I at the grain boundary not only experiences the distorted electron field, caused by the V_{Ti} in the cubic lattice, but also the highly disordered immediate crystal structure at the grain boundary. Therefore, it is reasonable that

the experimental value ΔE_Q of DB1 appears to be larger than the calculated value which is obtained by assuming the Fe_I at the center of the TiN lattice cubic in the bulk phase.

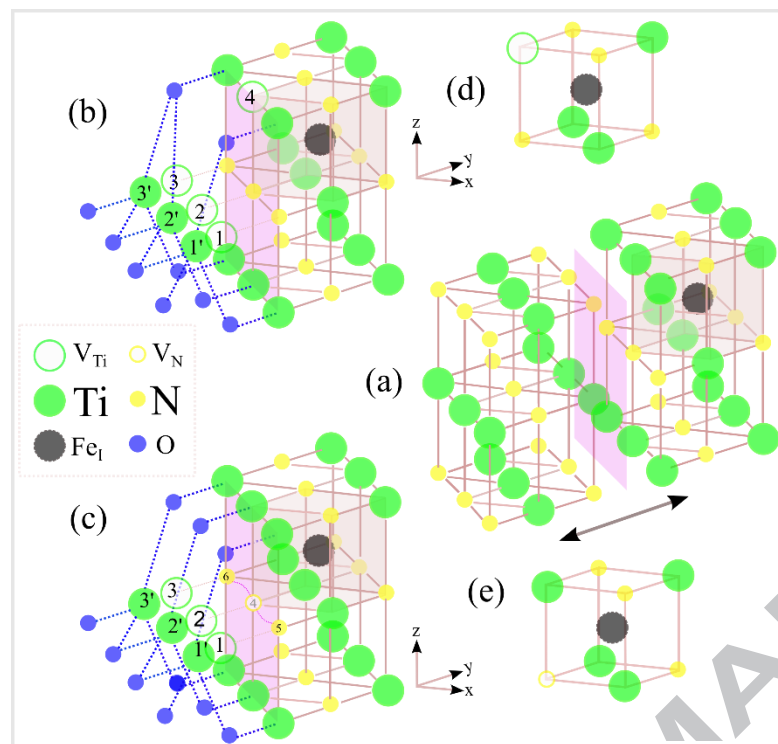


Fig. 6: Schematic illustration of the local lattice configuration and the unit cell structure of components (b) DB1 and (c) DB2, which represent the ^{57}Fe probe atom as interstitials located at the unit cell centers of TiN cubic structure with the (d) Ti vacancy (V_{Ti}) and (e) N vacancy (V_N), respectively, at the grain boundaries interfaced along the (110) direction of TiN (100). The boundary interface (shaded in magenta color) is featured with the -O-Ti- bridging row oxide structure, where a row of surface Ti atoms of the TiN cubic has shifted outwards from the original lattice sites (1, 2, 3) to the surface oxide sites (1', 2', 3') as discussed in Ref. [43]. The oxide-free interface in (110) plane between the two ideally Ti:N (1:1) terminated grains is shown in (a) as a comparison. Comparing to the ideal case in (a), the electron field distortion experienced by the Fe_I in the cubic center with a V_{Ti} at position 4 in (b) is enhanced by the highly-reconstructed oxide structures at the grain boundaries. In contrast, V_N -induced lattice distortion experienced by the Fe_I in the cubic center with a V_N at position 4 in (c) is neutralized by the nearest metastable N_I from position 5 or 6, which can be partially released under the -O-Ti- bridges from the Ti-N bond upon oxidation of Ti atom [43]. Solid green, black and yellow circles represent Ti lattice atoms, interstitial ^{57}Fe atoms in the cubic unit cell center and N lattice atoms, respectively. Void yellow and green circles represent V_N and V_{Ti} , respectively. Solid blue circles represent the surface O atoms in the surface oxide at the grain boundaries. Note: the ^{57}Fe should be treated as ^{57}Mn in the context of immediate interaction of implanted atoms with the local crystal structures.

Likewise, DB2 can be assigned to interstitial Fe_I in the centre of a TiN cubic with V_N (#11 in Table 2) at the grain boundaries as shown in Figs.6(c) and (e). Owing to the presence of unbonded N sites (dangling N bonds) located at the TiN/oxide interface in the proximity of V_{Ti} , it is thermodynamically favorable [43] and plausible that an initial release of N atoms as N_I would take place at the TiN/oxide interface shortly after formation of an ultrathin oxide layer on TiN thin film (at RT) as shown in Fig.6(c). Many reports agree that a certain amount of N_2 remains trapped in the uppermost part of the oxidized layer formed [46] [47] [48] [49]. Only with increasing temperature [47] or with the growth of oxide layers [48] N_I is completely released from the surface, either as N_2 or by formation of NO gas [41] [50] [51]. With the possibility of excess N_I trapped at the grain boundaries [50], in contrast to the isolated V_N in the bulk structure, V_N at a grain boundary is likely to form a complex with N_I . This can explain that the measured ΔE_Q of DB2 appears to be smaller than the calculated value due to the possible refilling of V_N by N_I at the grain boundary.

Fig.6(c) illustrates the Fe_I located at the centre of the TiN cubic structure with a V_N (position 4) near the grain boundary where the N_I is shown in a metastable structure with tendency to bond to V_N site or to be released as N_2 or NO gas upon annealing [47] [51]. In this configuration, the unbalanced electron density caused by V_N in the TiN unit cell experienced by the Fe_I can be dynamically balanced to a certain extent by the nearby N_I at the grain boundaries. Therefore, it is reasonable that the actually measured ΔE_Q value of DB2 appears to be smaller than the calculated one, which assumes that the Fe_I is located in the N_I -free cubic centre of the TiN in the bulk phase.

Finally, as temperature increases, the structure defects at grain boundaries can be annihilated. Therefore, as shown in Fig. 2(b), the area fractions of DB1 and DB2 decrease with temperature.

Conclusions

With ^{57}Fe eMS by dilute implantation of ^{57}Mn and theoretical calculations, we obtained the atomic scale lattice defect structures in an ultrathin epitaxial TiN film grown on MgO (100), which have been overlooked by other macroscopic analysing tools [27]. Most ^{57}Fe atoms were found to substitute Ti in the TiN lattice adopting the valence state 2^+ , with the rest located at the grain boundaries as interstitials. A small percentage ($\sim 4\%$) of V_N is detected in the bulk-like crystalline grains in the TiN thin film. Based on the theoretical predictions and the experimental conditions, it is most likely that a small portion of N_I exists inside the crystalline grains in the TiN thin film, which can be thermally activated and diffuses in a form of N_2 dimer-like N-N pair to promote the N_I-V_N pair formation inside the crystal grains, thus leading to a dynamic site-exchange between the lattice-N atom and the V_N in the temperature range 540 -620 K. Above 813 K, the compensation of V_N with N_I inside the crystalline grains or annihilation of N_I at the grain boundaries are more favourable. Furthermore, the results enable identifying the specific structural defects at the grain boundaries, which are consistent with experimental observations and theoretical modelling of the atomic scale oxidation of TiN at the surface. V_{Ti} is only detected at the TiN grain boundaries at RT, which can be annealed out at temperature above 813 K. There is no strong evidence of ferromagnetism resulting from dilute implantation of $^{57}Mn/^{57}Fe$ or due to intrinsic structural defects in the film. This work demonstrates that emission Mössbauer spectroscopy, assisted by theoretical calculations, is a powerful tool to study the defects in TiN nanostructures as well as the possibility of defect-induced or dilute-ferromagnetism on an atomic scale.

Acknowledgments

This work was supported by the European Union Seventh Framework through ENSAR (Contract No. 262010). B. Qi, H. P. Gislason, S. Ólafsson and F. Magnus acknowledge support from the Icelandic Research Fund (Grant No. 110017021-23). A. Tarazaga Martín-Lueugo and A. Bonanni acknowledge the support by the Österreichische Forschungsgesellschaft – FFG (P841482), the Austrian Science Foundation – FWF (P26830) and the European Research Council – ERC (grant 227690). We also acknowledge the support provided by the RILIS and technical teams at ISOLDE-CERN and by the Federal Ministry of Education and Research (BMBF) through the grants 05K16PGA and 05K16S11.

References

- [1] P. H. Mayrhofer, C. Mitterer, L. Hultman and H. Clemens, "Microstructural design of hard coatings," *Progress in Materials Science*, vol. 51, pp. 1032-1114, 2006.
- [2] L. A. Dvorina and A. S. Dranenko, "Use of refractory compounds in microelectronics," *Powder Metallurgy and Metal Ceramics*, vol. 39, pp. 9-10, 2000.
- [3] N. Gururaj V., S. Jeremy L., N. Xingjie, K. Alexander V., S. Timothy D. and B. Alexandra, "Titanium nitride as a plasmonic material for visible and near-infrared wavelengths," *Optical Materials Express*, vol. 2, no. 4, pp. 478-489, 2012.
- [4] H. Allmaier, L. Chioncel and E. Arrigoni, "Titanium nitride: A correlated metal at the threshold of a Mott transition," *Phys. Rev. B*, vol. 79, no. 23, p. 235126, 2009.
- [5] G. Gagnon, J. F. Currie, G. Béique and J. L. Brebner, "Characterization of reactively evaporated TiN layers for diffusion barrier applications," *Journal of Applied Physics*, vol. 75, no. 3, pp. 1565-1570, 1994.
- [6] T. Hara, A. Yamanoue, H. Lio, K. Inoue and G. Washidz, "Properties of titanium nitride films for barrier metal in aluminum ohmic contact systems," *Japanese Journal of Applied Physics*, vol. 30, no. 7 T. Hara, A. Yamanoue, H. lio, K. Inoue, G. Washidzu, S. Nakamura, pp. 1447-1451, 1991.
- [7] A. Torgovkin, S. Chaudhuri, J. Malm, T. Sajavaara, J. Ilari and I. .. Maasilta, "Normal-Metal-Insulator-Superconductor Tunnel Junction With Atomic-Layer-Deposited Titanium Nitride as Superconductor," *Applied Superconductivity IEEE Transactions on*, vol. 25, no. 3, p. 1101604, 2015.
- [8] Z. -Y. Yang, Y. -H. Chen, B. -H. Liao and K. -p. Chen, "Room temperature fabrication of titanium nitride thin films as plasmonic materials by high-power impulse magnetron sputtering," *Opt. Mater. Express*, vol. 6, pp. 540-551, 2016.
- [9] G. A. Olson, Growth of titanium-nitride thin films for low-loss superconducting quantum circuits, University of Illinois at Urbana-Champaign, 2015.

- [10] C. Gong, H. Meng, X. Zhao, X. Zhang, L. Yu, J. Zhang and Z. Zhang, "Unique Static Magnetic and Dynamic Electromagnetic Behaviors in Titanium Nitride/Carbon Composites Driven by Defect Engineering," *Sci Rep.*, vol. 6, no. Jan 7, p. 18927, 2016.
- [11] C. Gong, C. Chao Yan, J. Zhang, X. Cheng, H. Pan, C. Zhang, L. Yu and Z. Zhang, "Room-temperature ferromagnetism evolution in nanostructured titanium nitride superconductors-the influence of structural defects," *J. Mater. Chem*, vol. 21, pp. 15273-15278, 2011.
- [12] U. Helmersson, M. Lättemann, J. Bohlmark and J. T. Gudmundsson, "Ionized physical vapor deposition (IPVD): A review of technology and applications," *Thin Solid Films*, vol. 513, no. 1-2, pp. 1-24, 2006.
- [13] Z. Zang, A. Nakamura and J. Temmyo, "Single cuprous oxide films synthesized by radical oxidation at low temperature for PV application," *Optics Express*, vol. 21, no. 9, pp. 11448-11456, 2013.
- [14] Z. Zang, "Efficiency enhancement of ZnO/Cu₂O solar cells with well oriented and micrometer grain sized Cu₂O films," *Appl. Phys. Lett.*, vol. 112, p. 042106, 2018.
- [15] S. -H. Jhi, S. G. Louie, M. L. Cohen and J. Ihm, "Vacancy Hardening and Softening in Transition Metal Carbides and Nitrides," *Phys. Rev. Lett.*, vol. 86, pp. 3348-3351, 2001.
- [16] M. Guemmaz, A. Mosser and J. C. Parlebas, "Electronic changes induced by vacancies on spectral and elastic properties of titanium carbides and nitrides," *J. Electron Spectroscopy and Related Phenomena*, vol. 107, p. 91, 2000.
- [17] A. Azadeh Jafari, Z. Ghoranneviss, A. Salar Elahi, M. Ghoranneviss, N. Fasihi Yazdi and A. Rezaei, "Effect of deposition conditions and post deposition anneal on reactively sputtered titanium nitride thin films," *Thin Solid Films*, vol. 578, pp. 31-37, 2015.
- [18] P. Gütllich, E. Bill and A. X. Trautwein, *Mössbauer Spectroscopy and Transition Metal Chemistry*, Berlin, Heidelberg: Springer, 2011, pp. 7-24.
- [19] K. Johnston, J. Schell, J. G. Correia, M. Deicher, H. P. Gunnlaugsson, A. S. Fenta, E. David-Bosne, A. R. G. Costa and D. C. Lupasc, "The solid state physics programme at ISOLDE: recent developments and perspectives," *J. Phys. G: Nucl. Part. Phys.*, vol. 44, pp. 1361-1471, 2017.
- [20] H. P. Gunnlaugsson, T. E. Mølholt, R. Mantovan, H. Masenda, D. Naidoo, W. B. Dlamini, R. Sielemann, K. Bharuth-Ram, G. Weyer, K. Johnston, G. Langouche, S. Ólafsson, H. P. Gislason, Y. Kobayashi, Y. Yoshida, M. Fanciulli and the ISOLDE Collaboration, "Paramagnetism in Mn/Fe implanted ZnO," *Appl. Phys. Lett.*, vol. 97, p. 142501, 2010.
- [21] R. Mantovan, H. Gunnlaugsson, K. Johnston, H. Masenda, T. Mølholt, D. Naidoo, M. Ncube, S. Shayestehaminzadeh, K. Bharuth-Ram, M. Fanciulli, H. Gislason, G. Langouche, S. Ólafsson, L. Pereira, U. Wahl, P. Torelli and G. Weyer, "Atomic-scale magnetic properties of truly 3d-diluted ZnO," *Adv. Electron. Mater.*, vol. 1, p. 1400039, 2015.

- [22] H. Masenda, D. Naidoo, K. Bharuth-Ram, H. P. Gunnlaugsson, K. Johnston, R. Mantovan, T. E. Mølholt, M. Ncube, S. Shayestehaminzadeh, H. P. Gislason, G. Langouche, S. Ólafsson and G. Weyer, "Lattice sites, charge states and spin-lattice relaxation of Fe ions in 57Mn+ implanted GaN and AlN," *Journal of Magnetism and Magnetic Materials*, vol. 401, pp. 1130-1138, 2016.
- [23] H. O. Kirsten. C. Pietzsch., "Mössbauer investigations of (Ti,Fe)N hard coatings," *Thin solid films*, vol. 288, pp. 198-201, 1996.
- [24] K. Burda, C. Dauwe, P. De Bakker, E. De Grave, P. Fornal and J. Stanek, "Mössbauer study of 57Fe ions implanted in Ti and TiN," *Journal of Applied Physics*, vol. 78, p. 5067, 1995.
- [25] G. Weyer and the ISOLDE Collaboration, "Mössbauer spectroscopy at ISOLDE," *Hyperfine Interactions*, vol. 129, pp. 371-390, 2000.
- [26] P. Blaha, K. Schwarz, G. K. Madsen, D. Kvasnicka and J. Luitz, WIEN2k, an augmented plane wave+ local orbitals program for calculating crystal properties, K. Schwarz, Ed., Techn. Universität Wien, 2001.
- [27] F. Magnus, A. S. Ingason, S. Olafsson and J. T. Gudmun, "Growth and in-situ electrical characterization of ultrathin epitaxial TiN films on MgO," *Thin Solid Films*, vol. 519, p. 5861–5867, 2011.
- [28] V. N. Fedoseyev, K. Bätzner, R. Catherall, A. H. M. Evensen, D. Forkel-Wirth, O. C. Jonsson, E. Kugler, J. Lettry, V. I. Mishin, H. L. Ravn, G. Wey and ISOLDE Collaboration, "Chemically selective laser ion source of manganese," *Nuclear Instruments and Methods in Physics Research Section B: Beam Interactions with Materials and Atoms*, vol. 126, no. 1-4, pp. 88-91, 1997.
- [29] W. K. a. L. J. Sham, "Self-Consistent Equations Including Exchange and Correlation Effects," *Phys. Rev. A*, vol. 140, p. A1133, 1965.
- [30] J. P. Perdew, J. A. Chevary, S. H. Vosko, K. A. Jackson, M. R. Pederson, D. J. Singh and C. Fiolhais, "Atoms, molecules, solids, and surfaces: Applications of the generalized gradient approximation for exchange and correlation," *Phys. Rev. B* 4, vol. 46, p. 6671, 1992.
- [31] F. Neese, "Prediction and interpretation of the 57Fe isomer shift in Mössbauer spectra by density functional theory," *Inorg. Chim. Acta*, vol. 337, pp. 181-192, 2002.
- [32] U. D. Wdowik and K. Ruebenbauer, "Calibration of the isomer shift for the 14.4-keV transition in Fe57 using the full-potential linearized augmented plane-wave method," *Phys. Rev. B*, vol. 76, p. 155118, 2007.
- [33] P. Dufek, P. Blaha and K. Schwarz, "Determination of the Nuclear Quadrupole Moment of 57Fe," *Phys. Rev. Lett.*, vol. 75, pp. 3545-3548, 1995.
- [34] H. P. Gunnlaugsson, "Spreadsheet based analysis of Mössbauer spectra," *Hyperfine Interact.*, vol. 237, p. 79, 2016.

- [35] H. P. Gunnlaugsson, R. Mantovan, H. Masenda, T. E. Møhlholt, K. Johnston, K. Bharuth-Ram, H. Gislason, G. Langouche, D. Naidoo, S. Ólafsson, A. Svane, G. Weyer and the ISOLDE Collaboration, "Defect annealing in Mn/Fe-implanted TiO₂ (rutile)," *J. Physics D: Applied physics*, vol. 47, no. 6, 2014.
- [36] A. S. Ingason, F. Magnus, J. S. Agustsson, S. Ólafsson and J. T. Gudmundsson, "In-situ electrical characterization of ultrathin TiN films grown by reactive dc magnetron sputtering on SiO₂," *Thin Solid Films*, vol. 517, no. 24, pp. 6731-6736, 2009.
- [37] L. Tsetseris, N. Kalfagiannis, S. Logothetidis and S. T. Pantelides, "Role of N Defects on Thermally Induced Atomic-Scale Structural Changes," *Phys. Rev. Lett.*, vol. 99, no. 12, p. 125503, 2007.
- [38] L. Tsetseris, N. Kalfagiannis, S. Logothetidis and S. T. Pantelides, "Structure and interaction of point defects in transition-metal nitrides," *Phys. Rev. B*, vol. 76, p. 224107, 2007.
- [39] D. G. Sangiovanni, B. Alling, P. Steneteg and L. Hult, "Nitrogen vacancy, self-interstitial diffusion, and Frenkel-pair formation/dissociation in B1 TiN studied by ab initio and classical molecular dynamics with optimized potentials," *PHYSICAL REVIEW B*, vol. 91, p. 054301, 2015.
- [40] H. Matzke, "Diffusion in Carbides and Nitrides: Unsolved Problems," *Defect and Diffusion Forum*, vol. 83, pp. 111-130, 1992.
- [41] L. Hultman, "Thermal stability of nitride thin films," *Vacuum*, vol. 57, pp. 1-30, 2000.
- [42] C. Ernsberger, J. Nickerson, T. Smith, A. E. Miller and D. Banks, "Low temperature oxidation behavior of reactively sputtered TiN by x-ray photoelectron spectroscopy and contact resistance measurements," *Journal of Vacuum Science & Technology A: Vacuum, Surfaces, and Films*, vol. 4, p. 2784, 1986.
- [43] J. Zimmermann, Atomistic modeling of the oxidation of titanium nitride and cobalt/chromium alloy surfaces, Universität Bremen: Produktionstechnik, 2009.
- [44] S. X. Wu, Y. J. Liu, X. J. Xing, X. L. Yu, L. M. Xu, Y. P. Yu and S. W. Li, "Surface reconstruction evolution and anatase formation in the process of oxidation of titanium nitride film," *J. Appl. Phys*, vol. 103, p. 063517, 2008.
- [45] U. Diebold, "The surface science of titanium dioxide, Surf. Sci. Reports 48, 53," *Surf. Sci. Reports 48, 53*, vol. 48, p. 53, 2003.
- [46] N. C. Saha and H. G. Tompkins, "Titanium nitride oxidation chemistry: An x-ray photoelectron spectroscopy study," *J. Appl. Phys.*, vol. 72, p. 3072, 1992.
- [47] I. Milošev, H. -H. Strehblow and B. Navinšek, "Comparison of TiN, ZrN and CrN hard nitride coatings: Electrochemical and thermal oxidation," *Thin Solid Films*, vol. 303, no. Milošev, H.-H. Strehblow, B. Navinšek,, p. 246, 1997.

- [48] F. Esaka, K. Furuya, H. Shimada, M. Imamura, N. Matsubayashi, H. Sato, A. Nishijima, A. Kawana, H. Ichimura and T. Kikuchi, "Comparison of surface oxidation of titanium nitride and chromium nitride films studied by x-ray absorption and photoelectron spectroscopy," *J. Vac. Sci. Technol. A*, vol. 15, p. 2521, 1997.
- [49] J. Torres, C. C. Perry, S. J. Bransfield and D. H. Fa, "Low-temperature oxidation of nitrated iron surfaces," *J. Phys. Chem. B*, vol. 107, p. 5558, 2003.
- [50] L. Hultman, J. -E. Sundgren, L. C. Markert and J. E. Greene, "Ar and excess N incorporation in epitaxial TiN films grown by reactive bias sputtering in mixed Ar/N₂ and pure N₂ discharges," *Journal of Vacuum Science & Technology A: Vacuum, Surfaces, and Films*, vol. 7, no. 3, p. 1187, 1988.
- [51] J. Graciani, J. F. Sanz, T. Asaki, K. Nakamura and J. A. Rodriguez, "Interaction of oxygen with TiN(001): N-O exchange and oxidation process," *J. Chem. Phys.*, vol. 126, p. 244713, 2007.

Highlights:

- ^{57}Fe Mössbauer spectroscopy at truly dilute level ($<10^{-3}$ at%) is applied.
- An ultrathin epitaxial TiN thin film structure is studied.
- Theoretical calculations are provided to assist the analysis of the experimental measurement results.
- The structure and mobility of the lattice defects in the TiN film are probed at atomic scale.